energies

Article

Sand-Carrying Law and Influencing Factors in Complex Fractures of Nano-Clean Fracturing Fluid

Hongkai Han [1,2,3], Zhaoqi Shi [1], Weiqin Zuo [1,2,3,*], Shengjie Wu [1], Yanwei Liu [1,2,3], Kunrong Xie [1], Liqun Long [1] and Hani Mitri [4]

1 School of Safety Science and Engineering, Henan Polytechnic University, Jiaozuo 454000, China
2 Henan International Joint Laboratory of Coal Mine Safety and Occupational Hazards Prevention and Control, Henan Polytechnic University, Jiaozuo 454000, China
3 State Key Laboratory Cultivation Base for Gas Geology and Gas Control, Henan Polytechnic University, Jiaozuo 454000, China
4 Department of Mining and Materials Engineering, McGill University, Montreal, QC H3A0E8, Canada
* Correspondence: zuoweiqin@163.com

Abstract: Nano-clean fracturing fluids have broad application potential in coalbed methane reservoir fracturing owing to their high stability, good temperature resistance, low filtration loss, and strong frictional resistance reduction. However, the sand-carrying regularity of nano-clean fracturing fluids in coalbed methane reservoirs is unclear, especially for complex fractures with variable directions. This study established a sand transport model that considers proppant collision, wall friction blocking, fracture fluid filtration loss, and the fracture branching angle to study the sand-carrying law of nano-clean fracturing fluids and its influencing factors in complex fractures. The degrees of influence on equilibrium height and placement rate from high to low were the proppant particle size, proppant density, fracturing fluid properties, sand ratio, and pumping discharge volume, and the correlation degrees obtained by grey correlation analysis are 0.862, 0.861, 0.855, 0.854, and 0.832, respectively. As the complexity of the fractures deepens and the resistance increases, the flow rate of the fracturing fluid is reduced, making it difficult for the proppant to enter the branching joints. The sand-carrying performance of a nano-clean fracturing fluid is better than that of a common clear-water fracturing fluid. The fluid-structure coupling model of a nano-clean fracturing fluid can accurately characterize the sand-carrying law of nano-clean fracturing fluids, providing a research basis for optimizing high efficiency sand-carrying fracturing fluid parameters in coalbed methane reservoir fracturing construction.

Keywords: clean fracturing fluid; nanoparticles; sand-carrying law; complex fractures

check for updates

Citation: Han, H.; Shi, Z.; Zuo, W.; Wu, S.; Liu, Y.; Xie, K.; Long, L.; Mitri, H. Sand-Carrying Law and Influencing Factors in Complex Fractures of Nano-Clean Fracturing Fluid. *Energies* **2023**, *16*, 6056. https://doi.org/10.3390/en16166056

Academic Editors: Reza Rezaee and Pål Østebø Andersen

Received: 29 June 2023
Revised: 1 August 2023
Accepted: 8 August 2023
Published: 18 August 2023

1. Introduction

Coalbed methane (CBM) is a new energy with a high calorific value. However, unconventional natural gas differs from conventional natural gas in its mode of occurrence, reservoir formation mechanism, and reservoir characteristics [1–3]. Generally, it has three "low" characteristics: low saturation, permeability, and reservoir pressure. The method of coalbed methane extraction is different from that of traditional natural gas [4]. It requires reservoir modification methods such as hydraulic fracturing, gas injection to increase production, and heat injection to increase production [5–9]. Hydraulic fracturing is the most widely used method to fracture the target formation. It uses the fracturing fluid to carry the proppant into the fracture, ensuring that the fracturing fluid returns to the formation to create a strong conductivity of the sand-filled fracture and achieving an economical and practical extraction. Therefore, the choice of the fracturing fluid directly determines whether the proppant can effectively fill the fracture.

Alotaibi et al. [10] studied the sand-carrying law of slick water fracturing fluid in complex fractures and confirmed that it could carry proppant into multistage fractures and form sand-filled fractures with a specific inflow capacity. Zhang et al. [11] found that the inlet location significantly influences proppant placement, and the proppant transport capacity can be enhanced by increasing the jet velocity and decreasing the proppant density. Shi et al. [12] found that the fracture spacing and proppant concentration of the injected slurry significantly affected the extension path of the subsequently formed fractures. Fredd et al. [13] reported that a foam fracturing liquid system was superior to ordinary fracturing fluids for improving permeability. Tong et al. [14] found that the proppant spreads more uniformly under the carrying action of a foam fracturing fluid, and the faster the foam drains, the more uneven the final proppant spread is. Wang et al. [15] discussed a new thermosensitive in situ proppant based on the liquid-solid conversion of a supramolecular self-propelled fracturing fluid, and the results showed that the supramolecular self-propelled fracturing fluid had good fluidity and low damage to the reservoir. Li et al. [16] developed a clean fracturing fluid with less damage to the reservoir. Yang et al. [17]. found that a clean fracturing fluid can improve the permeability of the reservoir and the conductivity of fractures, thus improving the recovery rate of coalbed methane. Crews et al. [18] developed a modified nano-clean fracturing fluid that could effectively improve the filtration rate of fracturing fluid. Nettesheim et al. [19] studied the influence of nanoparticles on the performance of a clean fracturing fluid and found that adding a small amount of silica nanoparticles effectively improved the viscosity and viscoelasticity of the system. The members of this paper studied the laws of proppant migration and placement carried by clean fracturing fluid and the influence of fracturing fluid on the coal pore structure [9].

In summary, the current proppant transport law research mainly focuses on conventional clear-water fracturing. However, the clear-water fracturing fluid has poor rheology, large filtration loss, and a small fracturing range, which limits the extension of fracturing fractures; the overall fracturing efficiency is low, and the fracturing effect is not ideal. Moreover, the water viscosity is low, the sand-carrying performance is weak, the filtration loss is significant, and a large amount of water entering the coal seam easily produces a water-lock effect, which shortens the adequate pre-pumping time of coalbed methane and reduces the recovery rate. The foam fracturing fluid has high viscosity, strong fracture-forming ability, and causes low damage to the reservoir; however, the stability and actual fracturing effect of the foam fracturing fluid are not apparent at present, the fracturing cost is high, and the operation is complex. Clean fracturing fluids exhibit good sand-carrying properties, low filtration loss, and no residue; however, they exhibit low viscosity, poor temperature resistance [20], and an insufficient sand-carrying capacity. The modification of clean fracturing fluids by adding nanoparticles can effectively improve the viscosity and temperature resistance of the system and reduce the friction resistance, thus improving the sand-carrying capacity of the proppant in the fracturing fluids [21,22]. Nano-clean fracturing fluids are a new type of fracturing fluid, and there are few studies on the proppant transport law of a nano-clean fracturing fluid. Its sand-carrying law is unclear, and most existing models do not consider the complex fracture branching angle, wall friction blocking, fracturing fluid filtration loss, or other factors. The influence of fracturing fluid rheology on the sand-carrying process is ignored, which deviates significantly from the actual situation.

Therefore, based on the Eulerian multiphase flow model and particle dynamics model, the author constructed a nano-clean fracturing fluid sand-carrying transport model while considering the above influencing factors and the rheology of the fracturing fluid and studied the sand-carrying laws in complex fractures with multi-angle and multi-size clean fracturing fluids, focusing on the sand-carrying effect under different pumping discharge volumes, sand ratios, proppant particle sizes, proppant densities, and rheological parameters. It can provide a specific research basis for optimizing the fracturing parameters of coalbed methane reservoirs and has great significance for the efficient and environmentally friendly development of coalbed methane.

2. Simulation Methods and Modeling

2.1. Mathematical Models

The flow of a sand-carrying fluid composed of proppant and nano-clean fracturing fluid in the fracture is a solid-liquid two-phase flow problem. The Euler-Euler method can be used to simulate the settlement and transport law of the nano-clean fracturing fluid-carrying proppant in the fracture.

The liquid-phase and solid-phase continuity equation is as follows:

$$\frac{\partial(\alpha_i\rho_i)}{\partial t} + \nabla\cdot(\alpha_i r_i v_i) = 0 \tag{1}$$

where α is the volume fraction; ρ is the density, kg/m^3; ∇ is the Hamiltonian operator; t is the time, s; v is the velocity, m/s; the subscript i denotes the phase; and s and l represent the solid phase and liquid phase, respectively.

The liquid-phase and solid-phase momentum equation is as follows:

$$\frac{\partial(\alpha_i\rho_i v_i)}{\partial t} + \nabla\cdot(\alpha_i\rho_i v_i v_i) = -\alpha_i\nabla p_i + \nabla\cdot\tau_i + \alpha_i\rho_i g - M_D + F_S \tag{2}$$

$$\tau_l = \alpha_l\mu_l\left(\nabla\cdot\vec{v}_l + \nabla\cdot\vec{v}_l{}^T\right) + \alpha_l(\lambda_l - \frac{2}{3}\mu_l)\nabla\cdot\vec{v}_l\bar{\bar{I}} \tag{3}$$

$$\tau_s = \alpha_s\mu_s\left(\nabla\cdot\vec{v}_s + \nabla\cdot\vec{v}_s{}^T\right) + \alpha_{sl}(\lambda_s - \frac{2}{3}\mu_s)\nabla\cdot\vec{v}_s\bar{\bar{I}} \tag{4}$$

where p is the partial pressure, Pa; τ is the shear stress tensor, Pa; M_D is the interphase momentum exchange coefficient, kg/(m^3·s); μ is the particle phase shear viscosity, P$_a$·s; λ is the particle phase volume viscosity, P$_a$·s; F_s is the collision force between solid-phase particles; and I is the unit tensor, N/m^2.

The F_s expression of the collision force between solid particles is as follows:

$$F_s = 2(1+e)\nabla(\alpha_s\rho_l(c_p^2)) \tag{5}$$

where e is the impact recovery coefficient of solid particles, and the value is 0.9; α_s is the particle volume fraction, %; and c_p is the pulsation coefficient of solid particles, m/s.

Considering the relatively high sand content in an actual fracturing operation, the collision and friction between particles may change the momentum and energy exchange between the solid and liquid phases. The particle dynamics theory that considers the interactions between particles is expressed as follows:

$$\frac{3}{2}\left[\frac{\partial(\alpha_s\rho_s\theta_s)}{\partial t} + \nabla\cdot\left(\alpha_s\rho_s\vec{v_s}\theta_s\right)\right] = \left(-\rho_s\bar{\bar{I}} + \bar{\bar{\tau_s}}\right)\nabla\vec{v_s} - \nabla(k_\theta\nabla\theta_s) - \gamma + \Phi \tag{6}$$

where θ_s is the particle temperature, which does not represent the temperature of hot and cold but rather a measure of particle pulsation speed, m^2·s^{-2}; $(-\rho_s\bar{\bar{I}} + \bar{\bar{\tau_s}})\nabla\vec{v_s}$ is the particle pulsation energy due to the shear stress of the particle phase; $(k_\theta\nabla\theta_s)$ is the dissipation of particle pulsation energy along the particle temperature gradient; k_θ is the particle temperature diffusion coefficient, kg·m^{-1}d·s^{-1}; γ is the energy dissipation rate of collisions between particles, which can be calculated according to the formula obtained by Equation (7) [23], kg·m^{-1}·s^{-3}; Φ is the interphase kinetic energy transfer due to particle velocity change, kg·m^{-1}·s^{-3}; e is the impact recovery coefficient of solid particles, g_0 is the radial distribution function; and d_s is the particle size.

$$\gamma = \frac{12(1-e_s^2)g_0}{d_s}\rho_s\alpha_s\theta_s^{3/2} \tag{7}$$

Euler's multiphase flow model considers solid particles as a pseudo-fluid phase and inevitably gives them fluid parameters, such as shear viscosity, which reflects the behavior of collision and friction between particles [24]. The shear viscosity of a solid, μ_s, consists of three components: collisional viscosity, $\mu_{s,col}$; dynamic viscosity, $\mu_{s,kin}$; and frictional viscosity, $\mu_{s,fr}$.

$$\mu_s = \mu_{s,col} + \mu_{s,kin} + \mu_{s,fr} \tag{8}$$

The solid viscosity is described using the particle dynamics and Schaffer models, and the solid viscosity model is expressed as follows:

$$\mu_s = \frac{4}{5}\varepsilon_s\rho_s d_p g_0(1+e)\sqrt{\frac{\theta_s}{\pi}} + \frac{10\rho_s d_p\sqrt{\theta_s\pi}}{96 g_0(1+e)}\left[1+\frac{4}{5}\varepsilon_s g_0(1+e)\right]^2 + \frac{P_{s,f}\sin\phi}{2\sqrt{I_{2D}}} \tag{9}$$

Among them, we have the following:

$$P_{s,f} = 0.05\left[(\varepsilon_s - \varepsilon_{s,\min})^2/(\varepsilon_{s,\max} - \varepsilon_s)^5\right] \tag{10}$$

$$g_0 = \left[1-\left(\frac{\varepsilon_s}{\varepsilon_{s,\max}}\right)^{\frac{1}{3}}\right]^{-1} \tag{11}$$

where the frictional stress, $P_{s,f}$, and the radial distribution function, g_0, are two important parameters for calculating the particle shear viscosity; $\varepsilon_{s,max}$ is the maximum solid-phase volume fraction, set to 0.63; $\varepsilon_{s,min}$ is the frictional accumulation limit; d_p is the particle diameter, m; and I_{2D} is the second invariant of the partial stress tensor.

For liquid-solid interactions, the liquid phase transfers many forces to the solid phase in the liquid-solid two-phase flow model, including the drag, pressure gradient, and buoyancy forces. In this study, we mainly considered the buoyancy, F_L, and drag, F_D, of the fracturing fluid and the virtual mass force, $F_{VM,}$ of the fluid phase, owing to the accelerated motion of the particle phase.

The interphase momentum transfer phase is calculated as follows:

$$M_D = F_D + F_{VM} + F_L \tag{12}$$

$$F_L = C_L\alpha_s\rho_s(v_l - v_s)\times(\nabla\times v_l) \tag{13}$$

$$F_D = \frac{1}{6}\pi d^3\frac{\beta|v_l - v_s|}{1-\alpha_l} \tag{14}$$

$$F_{VM} = C_{VM}\alpha_s\rho_l\left(\frac{dv_l}{dt} - \frac{dv_s}{dt}\right) \tag{15}$$

where C_L is the lift coefficient, which is considered to be 0.25; C_{VM} is the virtual mass force coefficient, which is 0.5; d is the particle phase diameter, m; α_s and α_l are the volume fractions of the solid phase and liquid phase, respectively; and v_l and v_s are the liquid-phase and solid-phase velocities, m/s, respectively.

On the basis of the conservation equations for the solid-liquid two-phase flow, the mathematical models that reflect the special properties of the fluid also need to be added. The flow of the sand-carrying fluid in the fracture is a typical solid-liquid two-phase turbulent flow; therefore, the turbulence theory should be used to characterize its flow characteristics. This study simulated the solid-liquid two-phase flow of nano-clean fracturing fluid into the fracturing fracture. The turbulence model is chosen as the k-ε standard model with the turbulent kinetic energy equation and the dissipation rate equation, respectively, as

$$\frac{\partial}{\partial t}(\alpha_l\rho_l k) + \nabla\cdot(\alpha_l\rho_l v_l k) = \nabla\cdot\left(\alpha_l\frac{\mu_t}{\sigma_k}\nabla k\right) + G_{k,l} + \prod\nolimits_k - \alpha_l\rho_l\varepsilon \tag{16}$$

$$\frac{\partial}{\partial t}(\alpha_l\rho_l\varepsilon) + \nabla\cdot(\alpha_l\rho_l v_l\varepsilon) = \nabla\cdot\left(\alpha_l\frac{\mu_t}{\sigma_\varepsilon}\nabla\varepsilon\right) + \alpha_l\frac{\varepsilon}{k}(C_1G_{k,l} - C_2\rho_l\varepsilon) + \prod\nolimits_\varepsilon \tag{17}$$

where k is the turbulent kinetic energy of the continuous phase, m^2/s^2; l represents the liquid phase; ε is the dissipation rate of turbulent kinetic energy, m^2/s^2; μ_t is the viscosity coefficient of the continuous phase, Pa·s; $\prod_k$, $\prod_\varepsilon$ is the exchange coefficient between solid and liquid phases, kg/(m·s^3); σ_k is the turbulent Prandtl number of energy k, uncaused, and takes the value of 1.0; σ_ε is the turbulent Prandtl number of ε, uncaused, and takes the value of 1.3; $G_{k,l}$ is the turbulent kinetic energy; and C_1 and C_2 are empirical constants, taking the values of 1.44 and 1.92, respectively.

A nano-clean fracturing fluid is a non-Newtonian fluid, and the relationship between its viscosity and shear rate is not linear. Non-Newtonian fluids exhibit shear-dilution properties, in which the viscosity decreases as the shear rate increases, thereby accelerating the proppant settlement rate. Therefore, for non-Newtonian fluids, a significant error occurs when calculating the settling velocity of a proppant using traditional methods. Using the consistency coefficient, k, and rheological index, n, of a power-law fluid to characterize the particle settling velocity in a non-Newtonian fluid, the Reynolds number of a non-Newtonian fluid can be expressed as follows:

$$N_{Rep} = \frac{\rho_f d_p^n V_p^{2-n}}{k} \tag{18}$$

where ρ_f is the fracturing fluid density, kg/m^3; d_p is the particle diameter, m; and V_p is the particle settling velocity, m/s.

Because the model must consider the effect of fracturing fluid elasticity, using the equation of motion of the power rate model to simulate the settling process of proppant particles within a highly viscoelastic solution, such as a nano-clean fracturing fluid, can lead to a significant difference between the calculated and actual results. Based on this, Zhang et al. [25] proposed a new model for calculating the proppant settling velocity through extensive physical modeling experiments that considered the elasticity of the fluid, the flow pattern of the fracturing fluid, and the nature of the proppant. Based on this, after the proppant particles are carried into the fracture by the fracturing fluid, the settlement movement of the proppant is different from the free settlement in the fluid because its speed is affected by the interaction between the particles, the retarding effect of the rough wall surface, and the filtration effect of the fracturing fluid. We propose using Equation (19) to describe the settling process of the proppant within the nano-clean fracturing fluid.

$$V_p = f_c f_w f_f V_F \left[\frac{g\left(\rho_p - \rho_f\right) d_s^{n+1}}{18k} \right]^{\frac{1}{3n-1}} \tag{19}$$

V_F is the settling velocity factor, as shown in Equation (20):

$$V_F = 0.0011^{\frac{2n}{3n-1}} \left[\frac{9\lambda\left(2n^2 + n + 1\right)}{k} \right]^{\frac{1}{3n-1}} \tag{20}$$

where g is the acceleration of gravity, m/s^2; ρ_p is the particle density, kg/m^3; d_s is the proppant sieve particle size, m; f_c is the correction coefficient of the sand ratio; f_f is the positive coefficient of filtration disrepair; and f_w is the wall correction coefficient.

The settlement of proppant particles in fractures is affected by the interaction between the particles which is a complex dynamic motion caused by collisions or friction. This interference becomes more significant as the proppant to sand ratio increases. In addition, the proppant particles themselves have a specific viscosity, and an increase in the sand ratio increases the overall viscosity of the sand-carrying fluid, thereby increasing the resistance of the particles to sinking. The effect of the sand ratio on proppant interference settlement can be corrected using the sand-concentration correction factor:

$$f_c = (1 - c)^m \tag{21}$$

where c is the sand ratio in the carrying fluid, and m is an empirical constant related to the Reynolds number of the sand carrier fluid.

Most fractures formed by onsite fracturing are very narrow, with a width of approximately a few millimeters, and there are many small-scale and discontinuous distributions of rough surfaces on the fracture surface. Therefore, when propagating particles settle freely in the fracture, the wall squeezes the proppant particles, increasing the collision between particles and the friction between the particles and the flow channel. Thus, the kinetic energy loss of the particles increased, and the settlement of the particles was hindered. The wall-effect correction coefficient, f_w, can be used to express the influence of the wall surface of conventional cracks on the settlement rate as follows:

$$\frac{f_w - f_\infty}{f_0 - f_\infty} = \left[1 + \left(\frac{\lambda}{A}\right)^2\right]^B \tag{22}$$

where λ is the ratio of proppant particle diameter to fracture width (ball diameter ratio) without dimensionality; A is the fitting parameter, which is dimensionless and generally equals 0.64; B is the fitting parameter that has no dimensionality and is generally -0.98; and f_0 is the approximate value of the wall factor when the spherical diameter ratio tends to zero, and its general value is 0.001.

When the fracturing fluid flows in the fracture, the pressure difference between the inside and outside of the fracture causes the fracturing fluid to filter out to the formation, which not only causes the fracturing effect to deteriorate but also increases the fracturing construction cost and affects the proppant settlement rate. The positive coefficient, f_f, of filtration disrepair is calculated as follows:

$$f_f = \frac{1}{1 - \frac{C \cdot \sqrt{t_1}}{W}} \tag{23}$$

where C is the comprehensive filtration coefficient; t is time, s; and W is the seam width, m.

2.2. Boundary Conditions

The model was based on a pressure solver with a first-order windward format to discretize the control equations, and the SIMPLE algorithm was used to solve the algebraic system of equations. Setting the left inlet as the velocity inlet and the right outlet as the pressure outlet, and given the corresponding turbulence intensity and hydraulic diameter, the specific values were calculated according to the following equation:

$$I = 0.16(\mathrm{Re})^{-\frac{1}{8}} \tag{24}$$

The hydraulic radius calculation formula is

$$R_h = \frac{\omega H_0}{2(\omega + H_0)} \tag{25}$$

where ω is the inlet width, m; and H_0 is the inlet height, m.

The wall was chosen to have a no-slip boundary, and the tangential velocity and temperature generated by the proppant and wall were calculated using the Johnson-Jackson model with the following equations:

$$\frac{v_{sl}}{|v_{sl}|} \cdot \left(\tau_k + \tau_f\right) \cdot \omega + \frac{\phi \pi \rho_s g_0 \sqrt{\theta_s}}{2\sqrt{3}\alpha_s^{\max}} v_{sl} + \left(\omega \cdot \tau_f \cdot \omega\right) \tan \delta_w = 0 \tag{26}$$

$$\kappa_s \frac{\partial \theta_s}{\partial x} = \frac{\phi \pi |v_s| \rho_s \alpha_s g_0 \sqrt{\theta_s}}{2\sqrt{3}\alpha_s^{\max}} - \frac{\sqrt{3}\pi \rho_s \alpha_s g_0 \left(1 - e_w^2\right) \sqrt{\theta_s}}{4\alpha_s^{\max}} \theta_s \tag{27}$$

where v_{sl} is the slip velocity of the proppant particles at the wall, m/s; τ_k is the shear tensor generated by the proppant particles colliding with the wall, Pa; τ_f is the shear tensor generated by the proppant particles rubbing against the wall, Pa; w refers to the normal vector to the inner side of the wall; ϕ is the reflection coefficient, no factor, taking the value of 0.001; and δ_w is the friction angle between the proppant and the wall, rad, taking the value of $\pi/10$.

3. Model Verification and Simulation Experiment Scheme

3.1. Model Validation

Based on the similarity criterion, a fracture model with a size of 3000 mm × 400 mm × 10 mm was established, and two rectangular injection ports with a size of 20 mm × 10 mm were set on the left side of the fracture. The inlets were located at one-quarter of the fracture height and two-quarters of the fracture height. This inlet arrangement is conducive to increasing the proppant placement at the inlet end of the fracture and improving the connectivity between the borehole and the fracture [26]. In addition, a 20 mm × 10 mm rectangular outlet was set at the center of the right side of the fracture, and the model is shown in Figure 1.

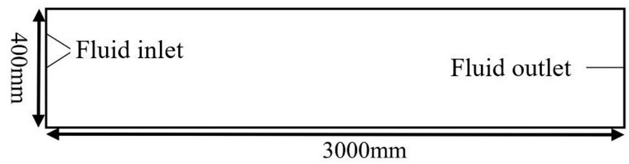

Figure 1. Numerical modeling of a fracture.

To ensure the quality of grid division and accuracy of calculation, a structured grid and positive hexahedral cells were used to grid the entire calculation area, and the grid was encrypted at the entrance; 171,864 grid cells were divided, and the final grid division is shown in Figure 2. According to the mathematical model in Section 2.1 and the boundary conditions in Section 2.2, the sand-carrying law of the clean fracturing fluid under the geometric model in Figure 1 was simulated and studied.

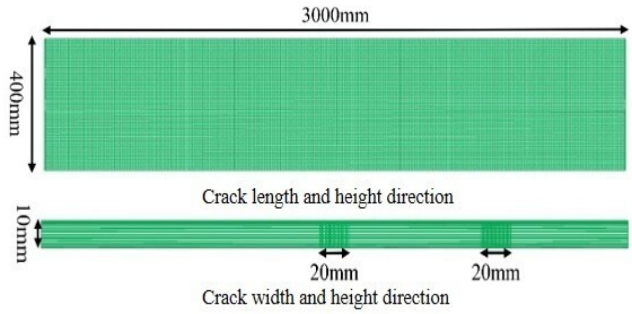

Figure 2. Schematic diagram of grid division.

The accuracy of the proposed model was verified through a comparison with previous experiments, using a large visualized flat-plate single-slit physical model [27]. A rectangular crack with a length, height, and width of 3000, 500, and 6 mm, respectively, was used for the experiment, with an inlet and outlet of the same size on the left and right sides of the crack with a width and height of 6 and 100 mm, respectively. A 30/50 mesh proppant particle (average particle size of 0.45 mm), proppant particles with a density of 2770 kg/m^3, sand ratio of 4%, and pump in discharge conversion speed of 2.31 m/s were selected for the experiment, and the numerical simulation parameters were set. A sand-laying profile was obtained when both parameters were balanced, consistent with the experimental parameter settings, as shown in Figure 3. The physical and numerical simulation results showed that the sand-laying profile distribution and equilibrium time were identical. This indicates that the established model describes the sand-carrying laws of fracturing fluid in a fracture.

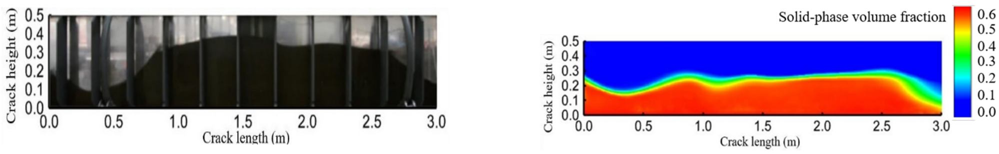

(**a**) (**b**)

Figure 3. Comparison of physical model and numerical model of sand-laying profiles. (**a**) Physical model of sand-laying profile. (**b**) Numerical model of sand-laying profile.

3.2. Simulation Experiment Scheme of Sand-Carrying Rule of Nano-Clean Fracturing Fluid under Different Factors

The controlled variable method was used to develop an experimental protocol from five aspects, namely the discharge volume, proppant density, proppant particle size, sand ratio, and fracturing fluid parameters, to discuss the changes in sand dike morphology when each factor was changed using the sand dike equilibrium height, equilibrium time, and laydown rate as parameters to characterize the sand dike morphology in the fracture. The experimental protocols are listed in Table 1.

Table 1. Experimental scheme.

Experimental Number	Discharge Volume/(m^3/min)	Proppant Particle Size/(mm)	Density /(kg/m^3)	Sand Ratio/(%)	Rheological Parameters
1#	0.084	0.45	1600	10	$\dot{\lambda} = 0.1$ s; $n = -0.3$; $\mu_0 = 1.0$
2#	0.062	0.45	1600	10	$\dot{\lambda} = 0.1$ s; $n = -0.3$; $\mu_0 = 1.0$
3#	0.104	0.45	1600	10	$\dot{\lambda} = 0.1$ s; $n = -0.3$; $\mu_0 = 1.0$
4#	0.084	0.67	1600	10	$\dot{\lambda} = 0.1$ s; $n = -0.3$; $\mu_0 = 1.0$
5#	0.084	0.30	1600	10	$\dot{\lambda} = 0.1$ s; $n = -0.3$; $\mu_0 = 1.0$
6#	0.084	0.45	1450	10	$\dot{\lambda} = 0.1$ s; $n = -0.3$; $\mu_0 = 1.0$
7#	0.084	0.45	2000	10	$\dot{\lambda} = 0.1$ s; $n = -0.3$; $\mu_0 = 1.0$
8#	0.084	0.45	1600	5	$\dot{\lambda} = 0.1$ s; $n = -0.3$; $\mu_0 = 1.0$
9#	0.084	0.45	1600	20	$\dot{\lambda} = 0.1$ s; $n = -0.3$; $\mu_0 = 1.0$
10#	0.084	0.45	1600	10	$\dot{\lambda} = 0.3$ s; $n = -0.3$; $\mu_0 = 1.0$
11#	0.084	0.45	1600	10	$\dot{\lambda} = 0.5$ s; $n = -0.3$; $\mu_0 = 1.0$
12#	0.084	0.45	1600	10	$\dot{\lambda} = 0.1$ s; $n = -0.4$; $\mu_0 = 1.0$
13#	0.084	0.45	1600	10	$\dot{\lambda} = 0.1$ s; $n = -0.5$; $\mu_0 = 1.0$
14#	0.084	0.45	1600	10	$\dot{\lambda} = 0.1$ s; $n = -0.3$; $\mu_0 = 2.0$
15#	0.084	0.45	1600	10	$\dot{\lambda} = 0.1$ s; $n = -0.3$; $\mu_0 = 3.0$

3.3. Simulation Experiment Scheme of Sand-Carrying Rule of Nano-Clean Fracturing Fluid in Complex Fracture

Owing to the severe inhomogeneity of coal seams and the development of natural fractures, many fractures are generated during the actual fracturing process, comprising main and branch fractures. During construction, the proppant enters not only the main fractures but also the branch fractures, and the transport law of the proppant in the branch fractures is equally essential. The complex fracture network formed by the interlocking of these fractures can effectively reduce the formation pressure and improve the reservoir conditions and provide sufficient inflow channels for subsequent CBM extraction. Therefore, to observe the placement pattern of the proppant in complex fractures more significantly, by establishing a multi-angle and multi-size complex fracture model and setting a larger proppant density and particle size to amplify the effect of clean fracturing fluid on sand dike morphology, the sand-carrying processes of clean fracturing fluid and conventional fracturing fluid in complex fractures were compared and analyzed, and the sand-carrying law of the clean fracturing fluid in the main fracture and branch fracture, respectively, was studied by using the preferred parameters, which can provide theoretical guidance for field fracturing.

3.3.1. Simulation Experiment Scheme of Sand-Carrying Rule for Y-Type Cracks

Three Y-type cracks were established, and the crack form was intersected by the main crack and a branch crack at 30°, 60°, and 90° angles, with the main crack set to the same size of 3000 mm × 400 mm × 10 mm as the single crack model in the previous section, and the branch crack size was set to 1800 mm × 400 mm × 5 mm, which is distributed in the middle of the main crack. The branch fracture with a 90° angle was simulated with clean-water fracturing fluid and nano-clean fracturing fluid. By contrast, the other branch fractures were only simulated with clean fracturing fluid. The inlet flow rate was set to 0.062 m^3/min; the proppant particle size was 0.63 mm, and the density was 2000 kg/m^3.

3.3.2. Simulation Experiment Scheme of Sand-Carrying Rule for Double-Y-Type Cracks

The double-Y crack pattern is a main crack intersected with branch joints at different distances on both sides, and the branch joints are distributed on both sides of the middle of the main crack, with one section of the branch joints set at the inlet end and the other section at the outlet end, and the dimensions of the main crack and branch joints are the same as those in the previous section.

3.3.3. Simulation Experiment Scheme of Sand-Carrying Rule for Well-Type Fracture

The well-type crack consists of one main crack and two orthogonal secondary branch joints, with two tertiary branch joints orthogonal to the secondary branch joints. The geometry of the main crack is consistent with that of the previous section. The dimensions of both the secondary and tertiary branch joints were set to 1800 mm × 400 mm × 5 mm, with the distance of the secondary branch joints from the entrance being 1.6 m and 1.8 m. The tertiary branch joints were parallel to the main joints and 450 mm away from them.

4. Results and Discussions

4.1. Influence of Different Factors on the Sand-Carrying Regularity of Nano-Clean Fracturing Fluid

4.1.1. Effect of Pumping Discharge Volume

Scenarios 2#, 1#, and 3# in Table 1 were selected to analyze the effect of the discharge volume on the proppant spreading morphology of the nano-clean fracturing fluid, and the sand dike morphology in equilibrium was obtained, as shown in Figure 4. The equilibrium parameters for the different discharges are listed in Table 2.

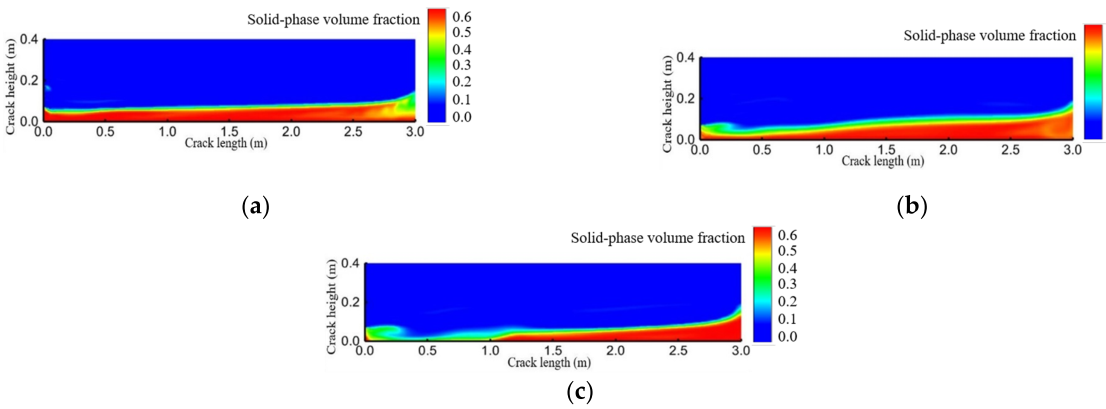

Figure 4. Effect of pumping discharge volume on sand dike morphology. (**a**) Pumping discharge volume of 0.062 m^3/min. (**b**) Pumping discharge volume of 0.084 m^3/min. (**c**) Pumping discharge volume of 0.104 m^3/min.

Table 2. Balance parameters at different pumping discharge volumes.

Pumping Discharge Volume/(m^3/min)	Balance Time/(min)	Balance Height/(cm)	Sand Dike Placement Rate/(%)
0.062	14.5	7.2	23.1
0.084	10.4	6.7	22.4
0.104	5.4	3.6	13.6

As can be seen in Table 2, with an increase in the pumping discharge volume, the equilibrium time decreases from 14.5 min to 5.4 min, a decrease of 62.7%; the equilibrium height decreases from 7.2 cm to 3.6 cm, a decrease of 50%; and the laydown rate decreases from 23.1% to 13.6%, a decrease of 41.1%. The transport power of the proppant particles in the fracture originates from the sand-carrying effect of the fracturing fluid. The variation in the construction discharge volume directly affects the sand-carrying rate of the fracturing fluid, thereby affecting the distribution of the proppant in the fracture. When the pumping discharge volume was 0.062 m^3/min, the fracture tail was less full, and more proppant settled at the entrance. With an increase in the pumping discharge volume, when the pumping discharge volume reaches 0.104 m^3/min, the proppant at 0–1 m of the fracture is in the shape of a "thin film", which indicates that less proppant is placed in the front part of the fracture. By contrast, the proppant content at the back end of the fracture increases significantly.

The experimental results show that the pumping rate is a crucial factor affecting the sand-carrying law of the fracturing fluid and plays a decisive role in the distribution pattern and movement trajectory of the proppant in the fracture. The increase in the pumping discharge volume causes an increase in the turbulence intensity at the inlet end of the main fracture. The vortex formed will involve more proppant at the depth of the fracture, while the settling proppant at the inlet end will be reduced. The unfilled area at the front end of the fracture also increases so that more proppant is transported to the depth of the fracture or even removed from the fracture. The larger the pumping discharge volume, the greater the amount of proppant that was carried out, and the corresponding equilibrium height of the sand dike was reduced. In addition, the larger the pumping discharge volume, the greater the amount of proppant that entered the crack per unit of time, thus decreasing the equilibrium time. Therefore, a low-pumping discharge volume method can be used when using a high-viscosity nano-clean fracturing fluid for fracturing construction.

4.1.2. Effect of Sand Ratio

Scenarios 8#, 1#, and 9# in Table 1 were selected to analyze the effect of the sand ratio on the proppant spreading morphology of the nano-clean fracturing fluid, and the sand dike morphology in the equilibrium state was obtained, as shown in Figure 5. The equilibrium parameters for the different sand ratios are listed in Table 3.

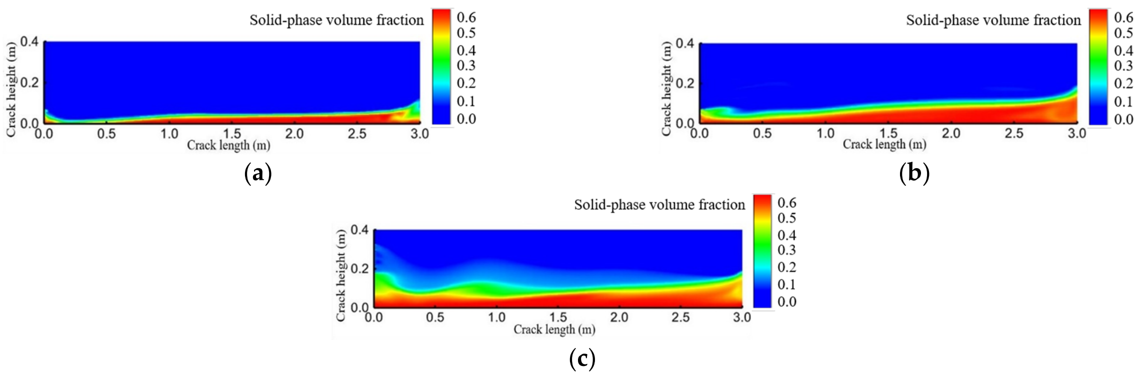

Figure 5. Effect of sand ratio on sand dike morphology. (**a**) Sand ratio of 5%. (**b**) Sand ratio of 10%. (**c**) Sand ratio of 20%.

Table 3. Equilibrium parameters at different sand ratios.

Sand Ratio/(%)	Balance Time/(min)	Balance Height/(cm)	Sand Dike Placement Rate/(%)
5	16.3	2.6	11.7
10	10.4	6.7	22.4
20	6.8	8.1	30.1

As seen in Table 3, the increase in the equilibrium height reached 157.7% when the sand ratio was increased from 5% to 10%, and the increase in equilibrium height was only 17.2% when the sand ratio was increased from 10% to 20%. The equilibrium time gradually decreased from 16.3 min to 6.8 min, with a decrease of 58.2%. Meanwhile, the laydown rate increased from 11.7% to 30.1% with an increase of 157.2% in the sand ratio. When the sand ratio increases from 10% to 20%, the growth rate of the height and placement rate of the sand dike decreases significantly because the settling of the proppant in the process of the fracturing fluid carrying sand disturbs the surrounding fracturing fluid, which will change its flow direction and hinder the settling of the proppant, which is aggravated with an increase in the sand ratio. In addition, the collision between proppant particles consumes a large amount of energy from the sand-carrying fluid, and the increase in the sand ratio aggravates the collision between particles, thus losing more kinetic energy and consuming more energy. Furthermore, the viscosity of the fracturing fluid increased owing to the addition of more solid particles, increasing the viscous drag on the proppant. More proppant was suspended above, with little change in the sand dike morphology.

The experimental results show that the sand ratio has a significant impact on the sand-carrying regularity of the fracturing fluid and the turbulence intensity formed at the entrance of the fracture by the nano-clean fracturing fluid with different sand ratios: the larger the sand ratio, the smaller the vortex and the lower the amount of proppant that is swept away, and the equilibrium height increases gradually as the sand ratio increases. In addition, the larger the sand ratio, the greater the amount of proppant that is involved in the fracture per unit time and the shorter the equilibrium time. When the sand ratio increases, the fracturing fluid carries more proppant into the fracture, the resistance of the fracturing fluid increases, and a large amount of proppant settles at the entrance, resulting in a deep fracture that cannot be effectively laid; in serious cases, the “sand plugging” phenomenon may occur. However, a minimal sand ratio weakens the conductivity of the fractures, and this is not conducive to improving oil recovery. It is essential to select a reasonable proppant-sand ratio; therefore, choosing a low sand ratio in the early stage of fracturing construction and a high sand ratio in the later stage of construction is recommended.

4.1.3. Effect of Proppant Particle Size

Scenarios 5#, 1#, and 4# in Table 1 were selected for analyzing the effect of the proppant particle size on the proppant spreading morphology of the nano-clean fracturing fluid, and the sand dike morphology in the equilibrium state was obtained, as shown in Figure 6. The equilibrium parameters for the different particle sizes are listed in Table 4.

As can be seen in Table 4, with an increase in the particle size, the equilibrium time was reduced from 14.5 min to 5.3 min, a decrease of 63.4%; the equilibrium height increased from 2.3 cm to 9.9 cm, an increase of 330%; and the laydown rate increased from 14.7% to 29.5%, an increase of 100.7%. As seen in Figure 6, when the proppant particle size increased from 0.3 mm to 0.67 mm, the height and placement rate of the sand dike increased significantly because the gravitational effect on the proppant particles strengthened with an increase in particle size. Although the turbulence intensity, buoyancy, and stagnation resistance of the fracturing fluid also increased during this process, their increase was still much lower overall than the increase caused by gravity, thus accelerating the proppant’s settling, which increased the equilibrium height of the sand dike.

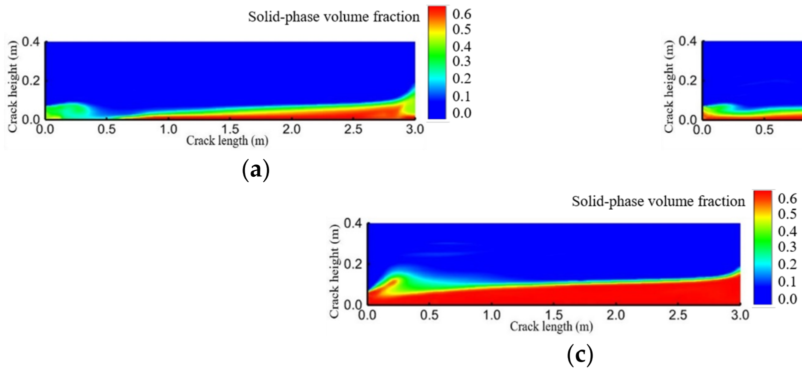

Figure 6. Effect of proppant particle size on sand dike morphology. (**a**) Proppant particle size of 0.3 mm. (**b**) Proppant particle size of 0.45 mm. (**c**) Proppant particle size of 0.67 mm.

Table 4. Equilibrium parameters of different particle sizes.

Grain Size/(m)	Balance Time/(min)	Balance Height/(cm)	Sand Dike Placement Rate/(%)
0.0003	14.5	2.3	14.7
0.00045	10.4	6.7	22.4
0.00067	5.3	9.9	29.5

The experimental results show that the proppant particle size significantly affects the sand-carrying regularity. A proppant with a small particle size is more easily transported to the distal end of the crack; however, the equilibrium height of the formed sand dike is lower, and a blank zone is easily formed at the front end of the crack. As the particle size of the proppant increased, the settling speed of the proppant accelerated, the height of the sand dike increased rapidly, and the flow of the sand-carrying liquid in the crack was blocked, which caused the subsequent proppant to settle more quickly near the entrance of the crack and caused the laying pattern of the sand dike to move toward the crack. Therefore, it is recommended to use a small-particle-size proppant in the early stage of fracturing and a large-particle-size proppant in the later stage to improve the fracturing effect.

4.1.4. Effect of Proppant Density

Scenarios 6#, 1#, and 7# in Table 1 were selected for the study to analyze the effect of the proppant density on the proppant spreading morphology of the nano-clean fracturing fluid, and the sand dike morphology in the equilibrium state was obtained, as shown in Figure 7. The equilibrium parameters at different densities are listed in Table 5.

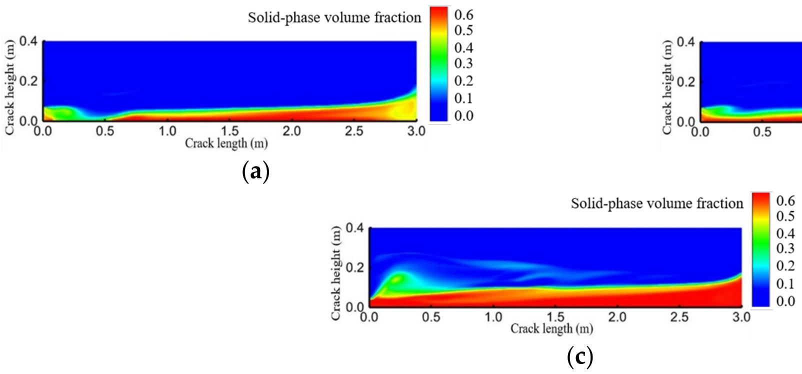

Figure 7. Effect of density on the morphology of sand dikes. (**a**) Proppant with a density of 1450 kg/m^3. (**b**) Proppant with a density of 1600 kg/m^3. (**c**) Proppant with a density of 2000 kg/m^3.

Table 5. Equilibrium parameters for different densities.

Proppant Density/(kg/m^3)	Balance Time/(min)	Balance Height/(cm)	Sand Dike Placement Rate/(%)
1450	13.9	3.0	16.8
1600	10.4	6.7	22.4
2000	6.2	9.7	29.1

As can be seen in Table 5, with an increase in proppant density, the equilibrium time was reduced from 13.9 min to 6.2 min, a decrease of 55.4%; the equilibrium height increased from 3.0 cm to 9.7 cm, an increase of 223.3%; and the laydown rate increased from 16.8% to 29.1%, an increase of 73.2%. Compared to Figure 7, under the same sand volume, the low-density proppant is laid less at both ends of the fracture. The blank zone is easily formed at the front end of the fracture. By contrast, the proppant is more uniformly laid in the fracture than in the medium-density and high-density proppants. This is due to the low gravity of the low-density proppant, as it improves the sand-carrying capacity of the nano-clean fracturing fluid and causes it to be suspended. Furthermore, the medium- and high-density proppants are subject to a greater gravity effect than the low-density proppant. They settle more in the fracture, whereas the low-density proppant is subject to a lower resistance effect and settles less in the fracture. A greater amount of proppant is carried out of the fracture by the fracturing fluid, resulting in the tail of the fracture. The proppant content at the end of the fracture was lower.

The experimental results show that the density of the proppant has a significant effect on the sand-carrying regularity, and the higher-density proppant particles with the same particle size are less likely to be swept to the fracture depth by the vortex formed near the inlet end and tend to settle near the inlet end. By contrast, the low-density proppant can easily carry to the fracture depth owing to its light mass, which enhances the carrying effect of the nano-clean fracturing fluid. Therefore, the equilibrium height gradually increases with an increase in proppant density. An increase in density accelerates the settling of the proppant, leading to the acceleration of sand dike piling and a decrease in the time required to reach the equilibrium height. Therefore, it is recommended to use a low-density proppant in the early stages of fracturing and a high-density proppant in the later stages to improve fracturing results.

4.1.5. Influence of Rheological Parameters

Rheological parameters such as the relaxation time, rheological index, and zero-shear viscosity in the fracturing fluid can affect the viscosity of the fracturing fluid and, thus, reflect the sand-carrying performance of the fluid. Therefore, 1#, 10#, 11#, 12#, 13#, 14#, and 15# in Table 1 were selected to analyze the effects of rheological parameters on the proppant spreading morphology of nano-clean fracturing fluids. The morphologies of the sand dikes at equilibrium are shown in Figures 8–10, and the equilibrium parameters are listed in Tables 6–8.

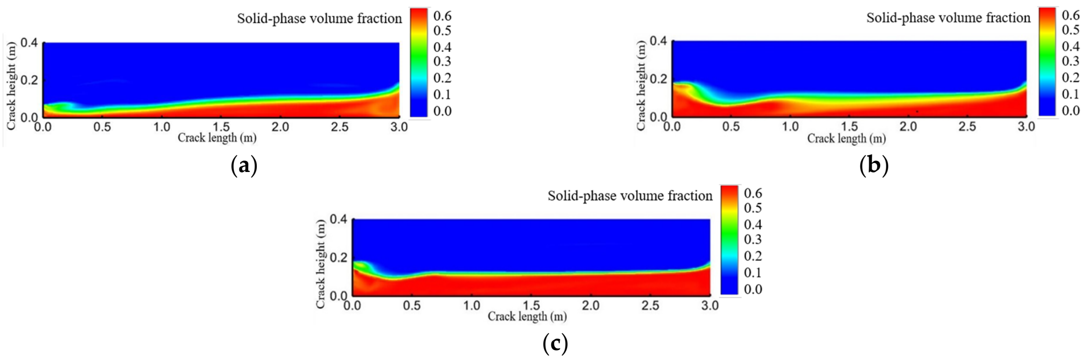

Figure 8. Effect of relaxation time on the morphology of sand dikes. (**a**) $\dot{\lambda} = 0.1$ s. (**b**) $\dot{\lambda} = 0.3$s. (**c**) $\dot{\lambda} = 0.5$ s.

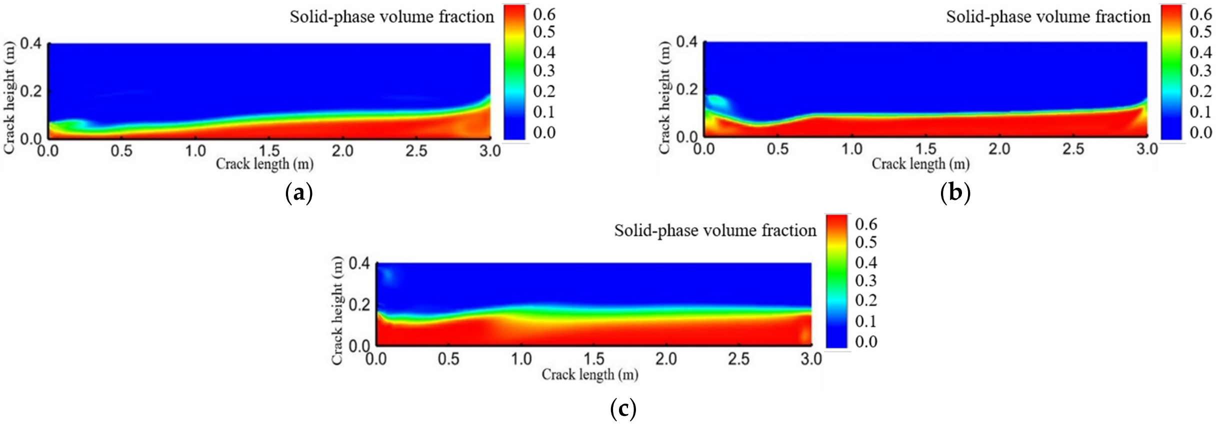

Figure 9. Effect of rheological index on the morphology of sand dikes. (**a**) n = −0.3. (**b**) n = −0.4. (**c**) n = −0.5.

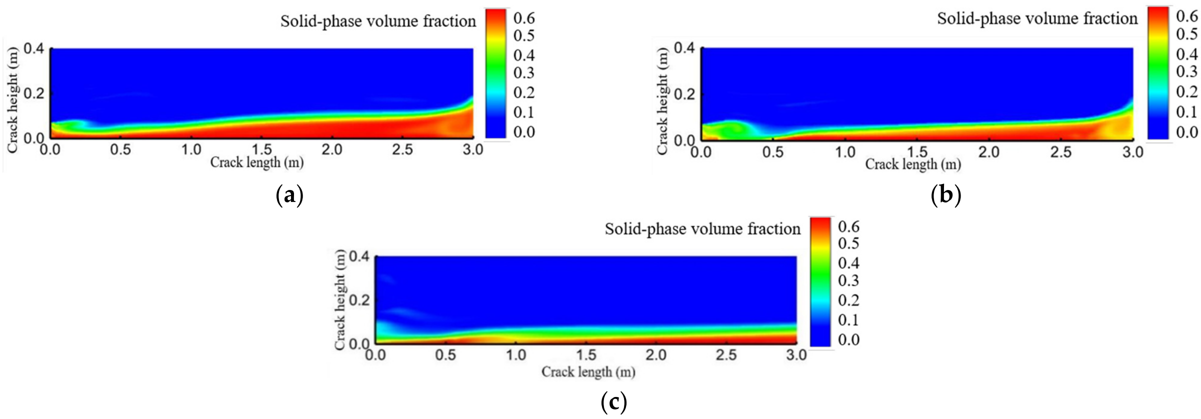

Figure 10. Effect of zero-shear viscosity on sand dike morphology. (**a**) $\mu_0 = 1.0$ Pa·s. (**b**) $\mu_0 = 2.0$ Pa·s. (**c**) $\mu_0 = 3.0$ Pa·s.

Table 6. Equilibrium parameters for different relaxation times.

Relaxation Time/(s)	Balance Time/(min)	Balance Height/(cm)	Sand Dike Placement Rate/(%)
0.1	10.4	6.7	22.4
0.3	8.2	9.6	30.3
0.5	4.3	12.1	32.8

Table 7. Equilibrium parameters for different rheological indices.

Rheology Index	Balance Time/(min)	Balance Height/(cm)	Sand Dike Placement Rate/(%)
−0.3	10.4	6.7	22.4
−0.4	6.8	8.4	24.7
−0.5	5.1	14.7	55.1

Table 8. Equilibrium parameters for different zero-shear viscosities.

Zero-Shear Viscosity μ_0 /(Pa·s)	Balance Time/(min)	Balance Height/(cm)	Sand Dike Placement Rate/(%)
1.0	10.4	6.7	22.4
2.0	11.1	1.9	16.2
3.0	12.6	1.7	15.1

(1) Effect of relaxation time

Scenarios 1#, 10#, and 11# in Table 1 were selected for the study to analyze the effect of the relaxation time on the proppant spreading morphology of the nano-clean fracturing fluid. As shown in Figure 8, with an increase in the relaxation time, the proppant content in the fracture increased, and the equilibrium height of the sand dike increased. The location where the equilibrium height appeared gradually approached the entrance, and many particles settled and gathered at the entrance, resulting in a gradual reduction in the proppant overflow area and easy sand plugging.

As can be seen in Table 6, with an increase in the relaxation time, the equilibrium time was reduced from 10.4 min to 4.3 min, a decrease of 58.6%; the equilibrium height increased from 6.7 cm to 12.1 cm, an increase of 80.6%; and the laydown rate increased from 22.4% to 32.8%, an increase of 31.7%.

(2) Effect of rheological index

Scenarios 1#, 12#, and 13# in Table 1 were selected for the study to analyze the effect of the rheological index on the proppant spreading morphology of the nano-clean fracturing fluid. Figure 9 shows that the height of the sand dike at the entrance gradually increased as the rheological index decreased and that the proppant was collected and settled at the entrance. The height of the sand dike in the horizontal direction increased with the increasing fracture length.

As can be seen in Table 7, with the reduction in the rheological index, the equilibrium time was reduced from 10.4 min to 5.1 min, a decrease of 50.9%; the equilibrium height increased from 6.7 cm to 14.7 cm, an increase of 119.4%); and the laydown rate increased from 22.4% to 55.1% (an increase of 145.9%).

(3) Effects of zero-shear viscosity

Scenarios 1#, 14#, and 15# in Table 1 were selected for the study to analyze the effect of the zero-shear viscosity on the proppant spreading morphology of the nano-clean fracturing fluid. As shown in Figure 10, when changing only the zero-shear viscosity of the nano-clean fracturing fluid, as the zero-shear viscosity increased, the horizontal carrying force and buoyancy of the proppant in the fracture increased. The settling rate of the proppant decreased, resulting in a lower sand dike height at the entrance. Overall, the higher the zero-shear viscosity, the lower the inlet sand dike height, the less prone it is to sand plugging, and the better the sand-carrying performance.

As can be seen in Table 8, with an increase in zero-shear viscosity, the equilibrium time increases from 10.4 min to 12.6 min, an increase of 21.2%; the equilibrium height decreases from 6.7 cm to 1.7 cm, a decrease of 74.6%; and the laydown rate decreases from 22.4% to 15.1%, a decrease of 32.5%.

With all parameters being the same, the smaller the relaxation time, the larger the critical shear rate of fluid shear thinning, the more stable the micelle structure of the fracturing fluid, and the stronger the sand-carrying capacity of the fracturing fluid (the rheological index reflects the characteristics of fluid shear thinning). The smaller the rheological index, the stronger the fluid behaves according to non-Newtonian laws; the larger the zero-shear viscosity, the higher the internal micelle entanglement strength of the fracturing fluid (the orderly arrangement of micelles forms a stable mesh structure) and the stronger the sand-carrying ability of the fracturing fluid. As shown in Figures 8–10, with an increase in zero-shear viscosity and a decrease in relaxation time, the equilibrium height of the sand dike decreased to a certain extent. The proppant moved deeper into the fracture. However, with a decrease in the rheological index, the shear-thinning characteristic of the fluid became more significant, the viscosity of the fracturing fluid inside the fracture decreased rapidly, the sand-carrying capacity weakened, and the proppant accumulated at the entrance.

4.1.6. Sensitivity Analysis of Influencing Factors

To analyze the degree of influence of each influencing factor on the sand-carrying law of the nano-clean fracturing fluid in the fracture, the equilibrium height, sand dike placement rate, and equilibrium time when the sand dike reached dynamic equilibrium were used as reference sequences, and correlation analysis samples were established separately for the grey correlation analysis to determine the degree of influence of each parameter on the morphology of the sand dike and provide a reference for optimizing the fracturing construction. The results of this analysis are shown in Figure 11.

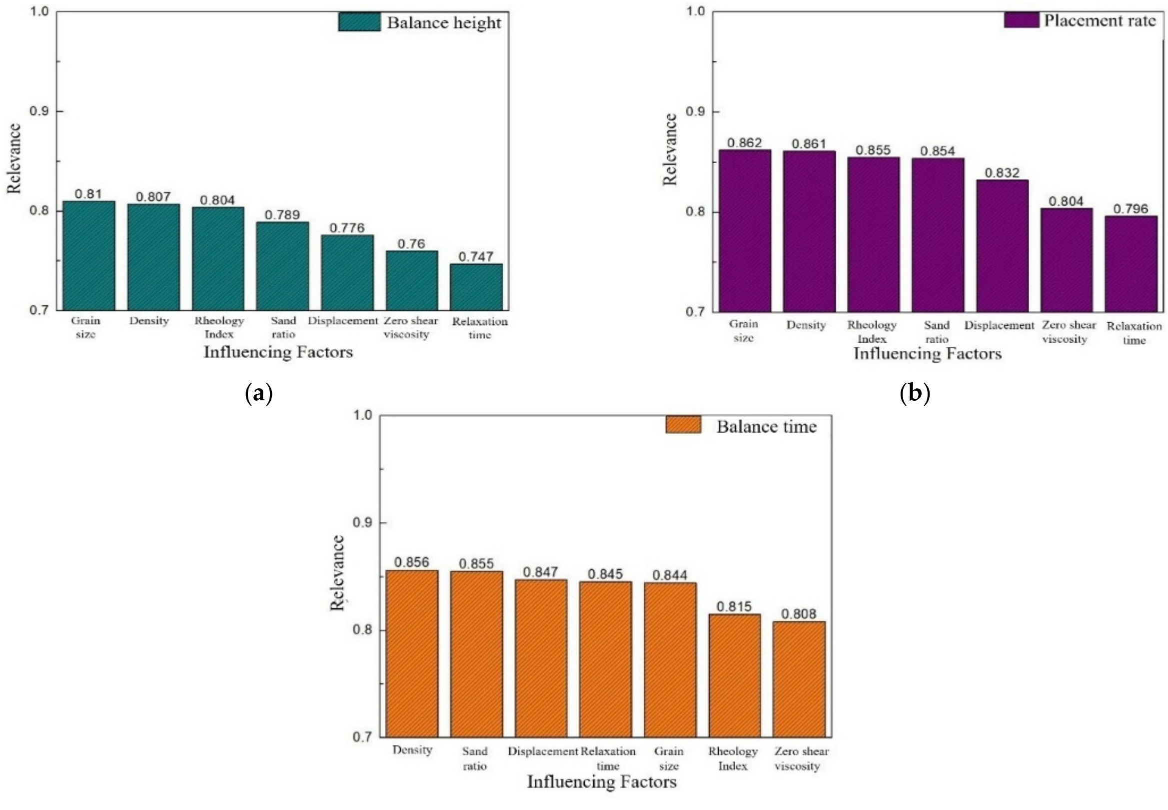

Figure 11. Correlation of each equilibrium parameter. (**a**) Balance height. (**b**) Placement rate. (**c**) Balance time.

As shown in Figure 11, the main factors influencing the equilibrium height and sand dike placement rate are relatively consistent. The degree of influence of each parameter from high to low is as follows: proppant particle size, proppant density, fracturing fluid properties, sand ratio, and discharge volume. The parameters of equilibrium time were the proppant density, sand ratio, discharge volume, fracturing fluid properties, and proppant particle size in descending order. Therefore, a large proppant particle size, high proppant density, and better rheological fracturing fluid significantly affect the equilibrium height and placement rate of the sand embankment and positively improve the fracture conductivity. A low proppant density, small sand ratio, and high displacement can significantly reduce the balance time of the sand bank, which is conducive to the migration of sandy fluid to deep fractures. In the actual construction, reasonable construction parameters can be selected according to the above sequence to ensure the effective placement of the proppant.

4.2. Analysis of Sand-Carrying Laws for Complex Cracks

4.2.1. Analysis of Sand-Carrying Laws of Y-Type Cracks

The Y-type fracture simulation scheme was simulated, and the results are shown in Figure 12. Figure 13 shows the volume distribution of the proppant in the main fracture and branch fracture with the branch fracture angle of 90°. When the fracturing fluid carries sand to the branch joints, the flow rate of the fracturing fluid in the main joints is reduced because part of the fracturing fluid flows into the branch joints, resulting in a poor sand-carrying performance for the fracturing fluid in the main joints and rapid settlement of the proppant. Comparing the sand-carrying performance of the nano-clean fracturing fluid and clean-water fracturing fluid in the main and branch joints, we see that the sand dikes formed in the main joints were more uniform. They had a higher placement rate than those of the clean-water fracturing fluid, and the proppant placement in the branch joints was also higher, indicating that the nano-clean fracturing fluid has a better transport effect in the branch joints, and this is an advantage of the nano-clean fracturing fluid compared with the conventional clean-water fracturing fluid.

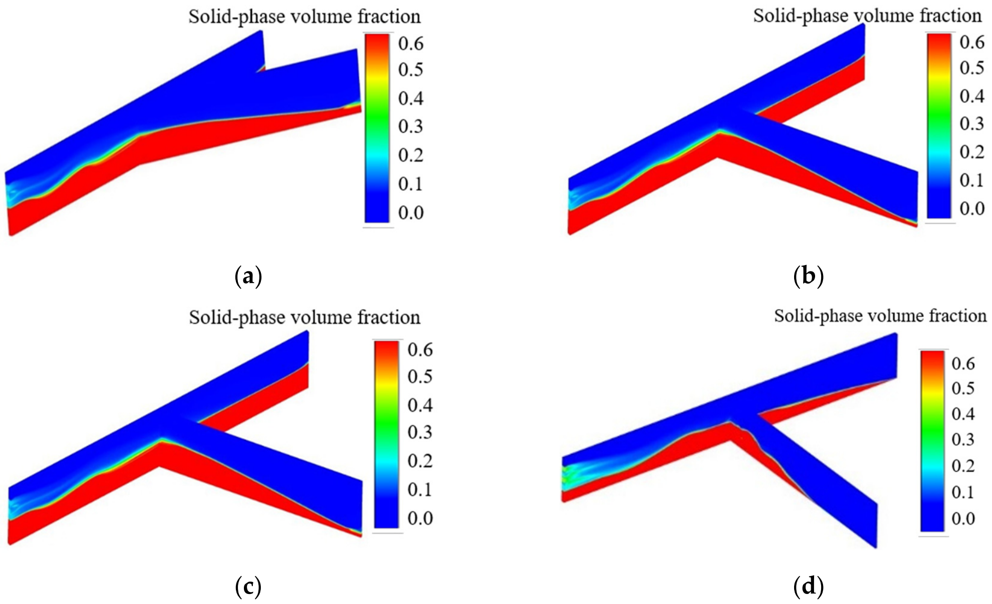

Figure 12. Y-type crack overall sand dike morphology: (**a**) 30° branch fracture nano-clean fracturing fluid, (**b**) 60° branch fracture nano-clean fracturing fluid, (**c**) 90° branch fracture nano-clean fracturing fluid, and (**d**) 90° branch fracture clear-water fracturing fluid.

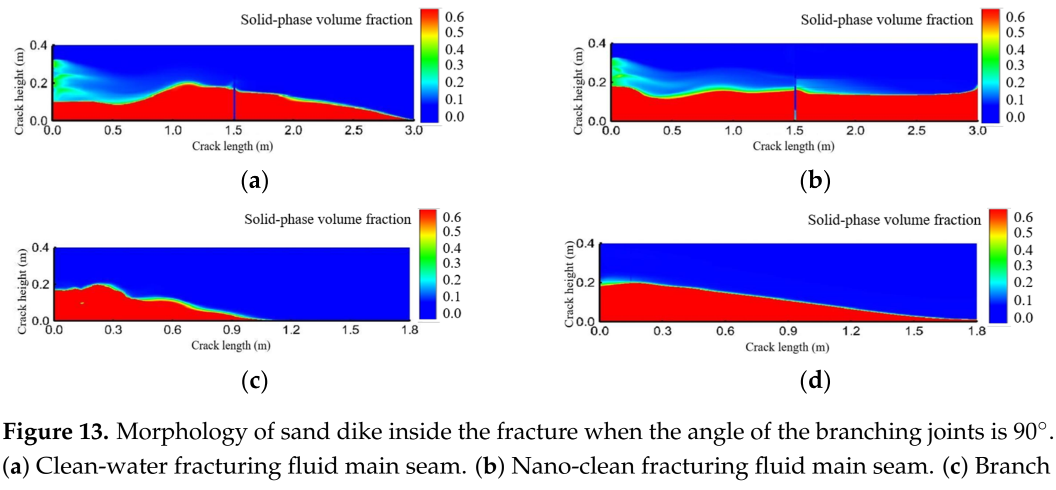

Figure 13. Morphology of sand dike inside the fracture when the angle of the branching joints is 90°. (**a**) Clean-water fracturing fluid main seam. (**b**) Nano-clean fracturing fluid main seam. (**c**) Branch joints of clean-water fracturing fluid. (**d**) Branch joints of nano-clean fracturing fluid.

Figure 14 shows the volume distribution of the proppant within the main and branch joints for branch joints at angles of 30° and 60°. Comparing the sand dike morphology formed at three different angles (30°, 60°, and 90°) of the fractures, we see that the proppant volume distribution in the main joints does not change at different angles. However, when comparing the sand placement in the branch joints at angles of 30° and 90°, the proppant placement can be observed in the tail of the branch joints at an angle of 30°. By contrast, almost no proppant is present in the tail of the branch joints at an angle of 90°. This indicates that the larger the angle between the branch joints and fractures, the greater the obstruction of the sand-carrying movement of the nano-clean fracturing fluid and the more difficult it is for the proppant to enter the branch joints.

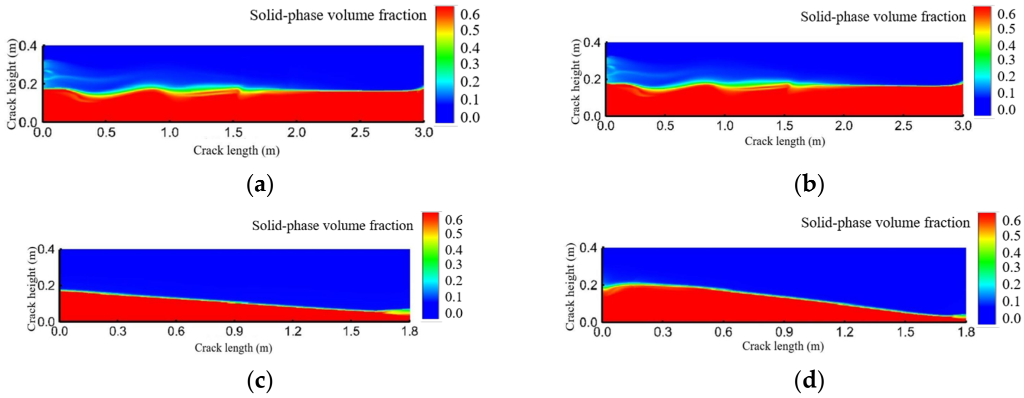

Figure 14. Morphology of sand dike inside the fracture when the angle of branching joints is 30° and 60°. (**a**) Main seam-laying pattern (30°). (**b**) Main seam-laying pattern (60°). (**c**) Branch seam-laying pattern (30°). (**d**) Branch seam-laying pattern (60°).

4.2.2. Analysis of Sand-Carrying Laws of Double-Y-Type Cracks

The double-Y-type crack simulation scheme was simulated, and the overall sand dike shape of the crack is shown in Figure 15. Figure 15 shows the morphological distribution of the overall sand dike for different fracturing fluids. It can be observed that the fracturing fluid carries the proppant particles to settle in the main fracture first. When the proppant is transported to the branch fracture and starts diverting, some proppant exists in both fractures. The sand-carrying fluid drove the transport of the proppant particles in the fracture, and the sand-carrying ability of the nano-clean fracturing fluid was better than that of the conventional fracturing fluid. Therefore, as shown in Figure 16, when the nano-clean fracturing fluid carries sand, the height of the sand dike at the entrance is lower, and sand plugging is less likely to occur. With an increase in time, the accumulation thickness of the sand dike in the horizontal direction increases slowly with the extension of the fracture. The equilibrium height position of the sand dike moves toward the distal end of the fracture. The sand dike formed by the sand-carrying action of the clean fracturing fluid is long and gentle. By contrast, the sand dike formed by the sand-carrying action of the clean-water fracturing fluid has a higher equilibrium height and a larger volume of sand dike in the entire fracture. However, the proppant placement at the end of the fracture is less and more nonuniform, and the equilibrium height and placement rate of the proppant in the branch fracture are lower than those of the clean fracturing fluid.

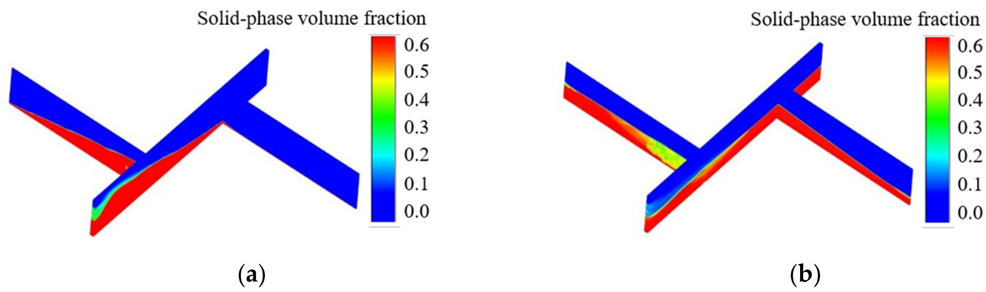

Figure 15. Double-Y-type cracks' overall sand dike morphology. (**a**) Clear-water fracturing fluid. (**b**) Nano-clean fracturing fluid.

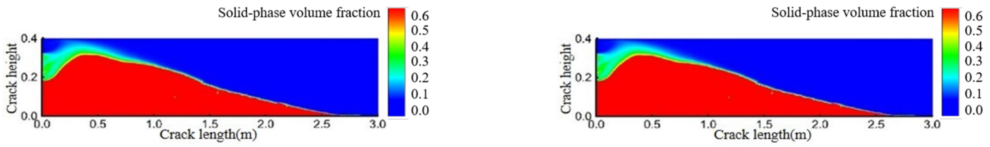

(**a**) (**b**)

Figure 16. Double-Y-type crack within the main seam sand dike morphology. (**a**) Clear-water fracturing fluid. (**b**) Nano-clean fracturing fluid.

Figure 17 shows that the proppant concentration in the distal branch fracture is much higher than that in the clear-water fracturing fluid. This phenomenon again proves that the sand-carrying performance of the nano-clean fracturing fluid is higher than that of the clear-water fracturing fluid. This is because the shear rate near the proximal branch is more significant than that in the distal branch, and the clean fracturing fluid has good rheology; thus, the apparent viscosity of the fracturing fluid in the proximal branch was low, and the proppant settled more. By contrast, the apparent viscosity was high in the distal branch, and the proppant settled less. When the clear-water fracturing fluid carried the fracturing fluid because the Newtonian fluid was not affected by the shear rate, the sand-carrying fluid first diverted into the proximal branch fracture, and the fluid in the main fracture continued to move in the fracture expansion direction. Moreover, when the sand-carrying fluid moves to the distal branch fracture again, the flow velocity in the fracture decreases because diversion has already occurred, which decreases the proppant concentration in the distal branch fracture.

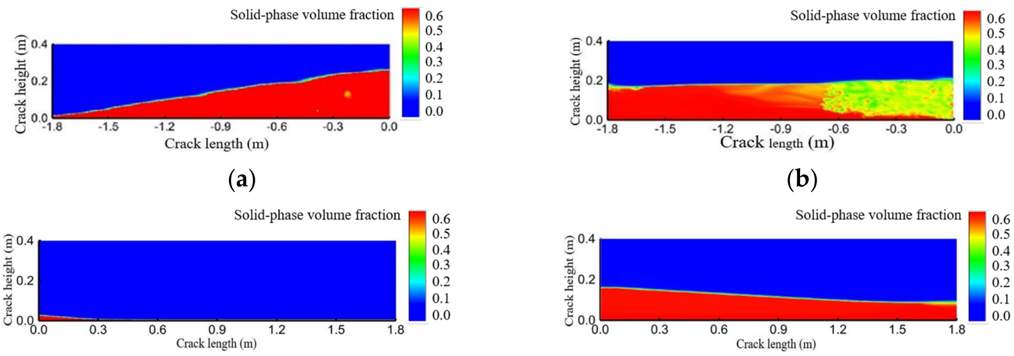

(**a**) (**b**) (**c**) (**d**)

Figure 17. Morphology of sand dike with branching joints within double-Y-type cracks. (**a**) Proximal branch joints of clean-water fracturing fluid. (**b**) Proximal branch joints of nano-clean fracturing fluid. (**c**) Distal branch joints of clean-water fracturing fluid. (**d**) Distal branch joints of nano-clean fracturing fluid.

4.2.3. Analysis of Sand-Carrying Laws of Well-Type Cracks

The overall sand dike morphologies of the cracks are shown in Figure 18. Comparing with the volume distribution of proppant in the main fracture in Figure 19, it can be seen that the sand dike formed under the carrying of clean water still shows a larger nonuniformity compared with the nano-clean fracturing fluid, but the nonuniformity is reduced compared with the double-Y fracture. The equilibrium time of the sand dike increases, and the equilibrium height decreases with an increase in fracture complexity, making it easier to form the sand dike accumulation at the end of the main fracture.

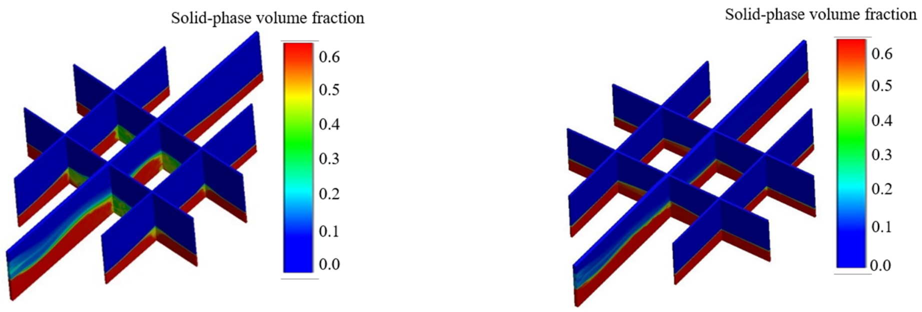

(**a**) (**b**)

Figure 18. Well-type crack overall sand dike morphology. (**a**) Clear-water fracturing fluid. (**b**) Nano-clean fracturing fluid.

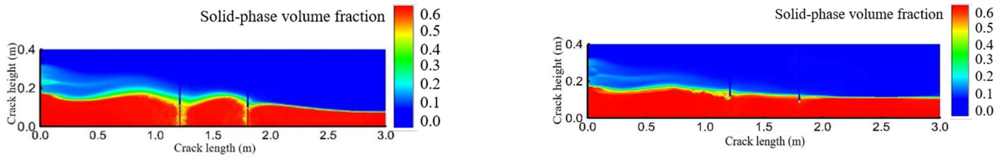

(**a**) (**b**)

Figure 19. Morphology of sand dike in the main seam of well-type crack. (**a**) Clear-water fracturing fluid. (**b**) Nano-clean fracturing fluid.

As can be seen in Figure 20, the proppant concentration in the secondary branch fracture was significantly higher than that in the clear-water fracture fluid. The placement rate in the proximal tertiary branch fracture was also slightly higher than that in the clear-water fracture fluid; however, the sand-carrying situation of both in the distal tertiary branch fracture was almost the same, which is because, under the sand-carrying situation of the clear-water fracture fluid, the sand dikes accumulated in the main fracture, which reduced the flow channels inside the complex fracture, and the fluid entered the branch fracture. This is because the accumulation of sand dikes in the main fracture reduces the flow channel inside the complex fracture and increases the fluid velocity into the branch fracture, partially suspending the proppant and moving it further into the fracture. In addition, both types of fracturing fluids formed sand dikes at a lower height in the branch joints away from the inlet than in the branch joints at the inlet. This can be mainly attributed to the presence of multiple fractures in the complex fracture for diversion, which reduces the fluid flow rate in the main fracture and causes the fracturing fluid to fail to meet the sand-carrying requirements, thereby accelerating the settlement of the proppant and allowing more fracturing fluid and proppant to enter the branch fracture near the entrance.

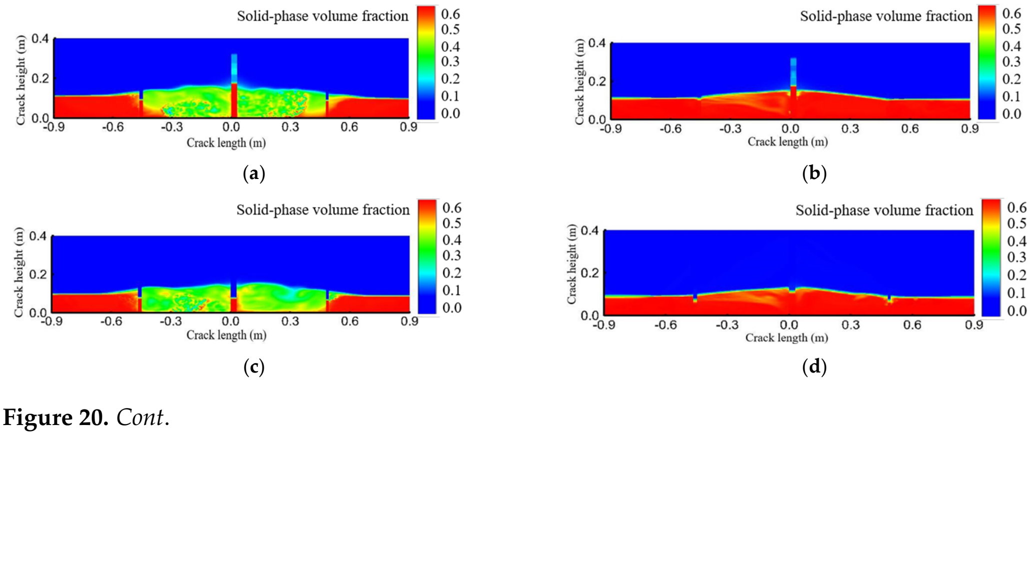

Figure 20. *Cont*.

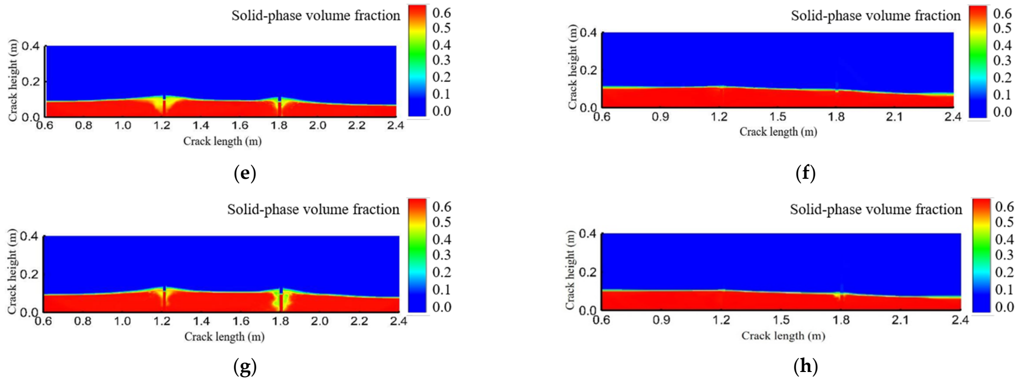

Figure 20. Morphology of sand dike in branching joints within well-type cracks. (**a**) Clear-water proximal secondary branch seam. (**b**) Nano-clean proximal secondary branch seam. (**c**) Clear-water distal secondary branch seam. (**d**) Nano-clean distal secondary branch seam. (**e**) Clear-water proximal tertiary branch seam. (**f**) Nano-clean proximal tertiary branch seam. (**g**) Clear-water distal tertiary branch seam. (**h**) Nano-clean distal tertiary branch seam.

5. Conclusions

(1) Nano-clean fracturing fluids are a new type of fracturing fluid that has a sand-carrying law that is unclear, especially for complex fractures with variable directions. The influence of fracturing fluid rheology, the complex fracture branching angle, or other factors on the sand-carrying process is ignored in the existing models, thus deviating significantly from the actual situation. A new nano-clean fracturing fluid sand-carrying transport model considering factors such as a mutual collision of the proppant, wall friction blocking, fracturing fluid filtration loss, and fracture branching angle was established which can accurately characterize the sand-carrying law of nano-clean fracturing fluid and provide a research basis for the optimization of fracturing construction parameters in coalbed methane reservoirs.

(2) Numerical simulations of the factors influencing the proppant placement pattern under the carrying action of nano-clean fracturing fluid were carried out using the controlled variable method. The grey correlation analysis was used to determine the ranking of the influence of each factor on the sand dike. The results showed that a large proppant particle size, high proppant density, and better rheological fracturing fluid significantly affect the equilibrium height and placement rate of the sand embankment and positively improve the fracture conductivity. A low proppant density, small sand ratio, and high displacement can significantly reduce the balance time of the sand bank, which is conducive to the migration of sandy fluid to deep fractures. In the actual construction, reasonable construction parameters can be selected according to the above sequence to ensure the effective placement of the proppant.

(3) A multi-angle and multi-size geometric model of complex fractures was constructed. A numerical simulation experiment of clean fracturing fluid in complex fractures was conducted to compare and analyze the experimental results of clean-water fracturing fluid and clean fracturing fluid, showing that an increase in the branching angle in complex fractures was not conducive to the sand-carrying of the fracturing fluid. The flow rate of the fracturing fluid would be reduced as the complexity of fractures increased, making it difficult for the proppant to enter the branching joints. However, the overall sand-carrying performance of the nano-clean fracturing fluid in the established complex fractures was better than that of the typical clear-water fracturing fluid, which promoted the application of the nano-clean fracturing fluid in CBM extraction. In this paper, the sand-carrying law of nano-clean fracturing fluid was studied under the assumption fracture, but the fractures generated by in situ fracturing have different trends and shapes, and the formation temperature also makes a difference. Therefore, it is necessary to carry out further research while considering the above influencing factors.

Author Contributions: All authors contributed to the conception and design of the study. W.Z. helped with the analysis through constructive discussions, which led to the idea of this study. Material preparation, data collection, and analysis were carried out by K.X. and L.L. H.H. proposed revisions through constructive discussion, and the first draft of the manuscript was written by H.H. and S.W. K.X. and Z.S. conducted the data analysis and visualized the experimental results to optimize the manuscript. Y.L. played a supervisory and leading role in the essay-writing process, and the accuracy and standardization of the paper's language was modified by H.M. All authors commented on previous manuscripts. All authors have read and agreed to the published version of the manuscript.

Funding: This paper was jointly funded by the National Natural Science Foundation of China, (grants No. 52104190, 52274188, and 52174173); the Outstanding Youth Foundation of Henan Polytechnic University (grant No. J2021-5); Strategic Research and Consulting Project of the Chinese Academy of Engineering (grant No. 2023HENZDB05); the Focus R&D and Promotion for Scientific and Technological Project of Henan Province (grant No. 222102320012); the Project Funded by China Postdoctoral Science Foundation (grants No. 2020M682291 and 2022T150194); and the State Key Laboratory Cultivation Base for Gas Geology and Gas Control (Henan Polytechnic University) (grant No. WS2021A05).

Data Availability Statement: Not applicable.

Conflicts of Interest: The authors declare that there are no conflict of interest.

References

1. Hou, J.; Wang, C.; Liu, P. How to improve the competiveness of natural gas in China with Energy Internet and "The Belt and Road Initiative". *Int. J. Energy Res.* **2018**, *42*, 4562–4583. [CrossRef]
2. Zhou, Y.; Lin, M. System simulation of air-cooling single effect LiBr absorption refrigerating system driven by solar heat source. *Environ. Earth Sci.* **2021**, *766*, 23–25. [CrossRef]
3. Zheng, C.; Jiang, B.; Xue, S.; Chen, Z.; Li, H. Coalbed methane emissions and drainage methods in underground mining for mining safety and environmental benefits: A review. *Process Saf. Environ. Prot.* **2019**, *127*, 103–124. [CrossRef]
4. Lu, Y.Y.; Zhang, H.D.; Zhou, Z.; Ge, Z.L.; Chen, C.J.; Hou, Y.D.; Ye, M.L. Current Status and Effective Suggestions for Efficient Exploitation of Coalbed Methane in China: A Review. *Energy Fuels* **2021**, *35*, 9102–9123. [CrossRef]
5. Wang, Y.; Lu, Y.; Li, Y.; Wang, X.; Yan, X.; Zang, Z. Progress and application of unconventional reservoir fracturing technology. *Acta Pet. Sin.* **2012**, *33*, 149–158.
6. Huang, Z.; Li, G.; Yang, R.; Li, G. Review and development trends of coalbed methane exploitation technology in China. *J. China Coal Soc.* **2022**, *47*, 3212–3238.
7. Chen, H.; Fan, H.; Guo, J.; He, X. Analysis and prospect of hydraulic fracturing fluids for coalbed methane Wells. *Coal Geol. Explor.* **2017**, *45*, 33–40.
8. Men, X.; Han, Z.; Gong, H.; Wang, Y. Challenges and Opportunities of CBM exploration and development in China under the new situation. *Nat. Gas Ind.* **2018**, *38*, 10–16.
9. Zuo, W.; Zhang, W.; Liu, Y.; Han, H.; Huang, C.; Jiang, W.; Mitri, H. Pore Structure Characteristics and Adsorption and Desorption Capacity of Coal Rock after Exposure to Clean Fracturing Fluid. *ACS Omega* **2022**, *7*, 21407–21417. [CrossRef]
10. Alotaibi, M.A.; Jennifer, L. Slickwater Proppant Transport in Hydraulic Fractures: New Experimental Findings and Scalable Correlation. *Miskimins Spe Prod. Oper.* **2018**, *3*, 164–178. [CrossRef]
11. Zhang, T.; Guo, J.; Liu, W. CFD simulation of proppant transport settlement behavior in clear water fracturing. *J. Southwest Pet. Univ.* **2014**, *36*, 74–82.
12. Shi, F.; Wang, X.; Liu, C.; Liu, H.; Wu, H. A coupled extended finite element approach for modeling hydraulic fracturing in consideration of proppant. *J. Nat. Gas Sci. Eng.* **2016**, *33*, 885–897. [CrossRef]
13. Fredd, C.N.; Olsen, T.N.; Brenize, G. Polymer-Free Fracturing Fluid Exhibits Improved Cleanup for Unconventional Natural Gas Well Applications. In Proceedings of the SPE Eastern Regional Meeting, Charleston, WV, USA, 15–17 September 2004.
14. Tong, S.; Singh, R.; Mohanty, K.K. A visualization study of proppant transport in foam fracturing fluids. *J. Nat. Gas Sci. Eng.* **2018**, *52*, 235–247. [CrossRef]
15. Luo, Z.; Zhang, N.; Zhao, L.; Pei, Y.; Liu, P.; Li, N. Innovative Encapsulating Acid with Release Dually Controlled by the Concentration of Hydrogen Ions and Temperature. *Energy Fuels* **2019**, *33*, 4976–4985. [CrossRef]
16. Li, T.; Yang, Q.; Feng, W.; Qian, Z.H.N. Indoor research and field application of a new type of clean fracturing fluid for coalbed methane. *Sci. Tech.* **2012**, *12*, 9828–9832.
17. Yang, F.; Ge, Z.; Zheng, J. Viscoelastic surfactant fracturing fluid for underground hydraulic fracturing in soft coal seams. *J. Pet. Sci. Eng.* **2018**, *169*, 646–653.
18. Crews, J.B.; Huang, T.; Wood, W.R. The Future of Fracturing-Fluid Technology and Rates of Hydrocarbon Recovery. In Proceedings of the SPE Annual Technical Conference and Exhibition, Denver, CO, USA, 21–24 September 2008.

19. Nettesheim, F.; Liberatore, M.W.; Hodgdon, T.K.; Wagner, N.J.; Kaler, E.W.; Vethamuthu, M. Influence of Nanoparticle Addition on the Properties of Wormlike Micellar Solutions. *Langmuir* **2008**, *24*, 7718–7726. [CrossRef]
20. Chen, H.; Fan, H.; Guo, J.; Tang, M.; Ni, F. Evaluation and Prediction of Coalbed Gas Fracturing Fluid. *Adv. Mater. Res.* **2014**, *1008*, 257–263. [CrossRef]
21. Dai, C.; Li, Y.; Xie, Q.; Xu, K.; Hu, Y.; Zhou, Z.; Wu, Y. Reduction of clean fracturing fluid filtration loss by viscosity enhancement using nanoparticles: Is it feasible? *Chem. Eng. Res. Des.* **2020**, *156*, 414–424. [CrossRef]
22. Zhao, M.; Gao, Z.; Dai, C.; Sun, X.; Zhang, Y.; Yang, X.; Wu, Y. Effect of Silica Nanoparticles on Wormlike Micelles with Different Entanglement Degrees. *J. Surfactants Deterg.* **2019**, *22*, 587–595. [CrossRef]
23. Lun, C.K.K.; Savage, S.B.; Jeffrey, D.J.; Chepurniy, N. Kinetic theories for granular flow: Inelastic particles in Couette flow and slightly inelastic particles in a general flow field. *J. Fluid. Mech.* **1984**, *140*, 223–256. [CrossRef]
24. Yao, J.; Yang, Y.; Huang, Z.; Sun, J.; Wang, J.; Yang, Y. Influence of particle viscosity model on the flow behavior of ultra-dense particles simulated by Euler multiphase flow model. *CIESC J.* **2020**, *71*, 4945–4956.
25. Zhang, G.; Li, M.; Geng, K.; Han, R.; Xie, M.; Liao, K. New integrated model of the settling velocity of proppants falling in viscoelastic slick-water fracturing fluids. *J. Nat. Gas Sci. Eng.* **2016**, *33*, 518. [CrossRef]
26. Zhan, Z. Study on the Law of Sand Transport of Slippery Water in Fractured Fracture. Master's Thesis, Xi'an Shiyou University, Xi'an, China, 2018.
27. Zhou, D.; Zhang, Z.; Hui, F. Experiment and numerical simulation on transportation laws of proppant in major fracture during slick water fracturing. *Pet. Drill. Tech.* **2017**, *39*, 499–508.